Supporting Information for: Nanostructured Topological State in Bismuth Nanotube Arrays: Inverting Parity Symmetry of Molecular Orbitals

Kyung-Hwan Jin,[†] Seung-Hoon Jhi,[‡] and Feng Liu[*,†,¶]

†*Department of Materials Science and Engineering, University of Utah, Salt Lake City, UT 84112, United States*

‡*Department of Physics, Pohang University of Science and Technology, Pohang 790-784, Korea*

¶*Collaborative Innovation Center of Quantum Matter, Beijing 100084, China*

E-mail: fliu@eng.utah.edu

S1. The notation of Bi-NTs

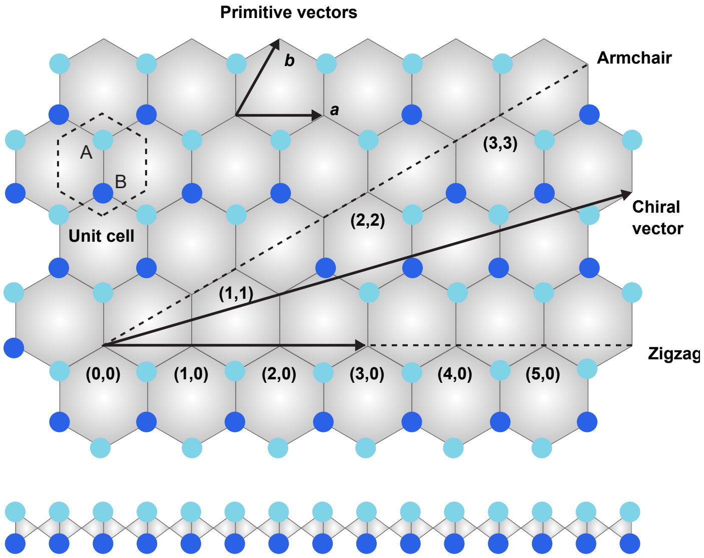

Figure S1: The hexagonal lattice of a single Bi bilayer and the notation of Bi-NTs. A Bi-NT is formed by rolling up a single Bi bilayer along a chiral vector. The atomic structure of a Bi-NT defined by the chiral indices, (n,m). If m=0, the nanotubes are called zigzag Bi-NT, and if n=m, the nanotubes are called armchair Bi-NT, in the same notation of carbon nanotubes. We defined the zigzag Bi-NTs as (n,0) Bi-NTs.

S2. The interaction strength of intertube coupling

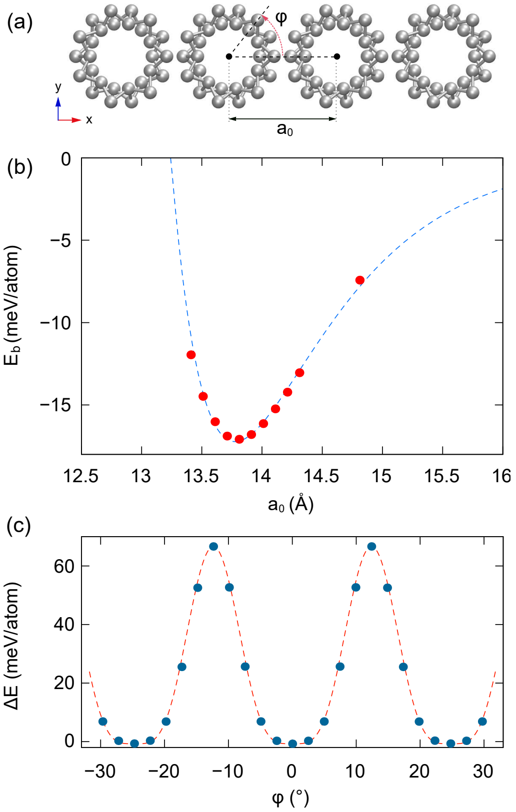

Figure S2: Interaction strength of intertube coupling in Bi-NT array. (a) Schematic cross-section view of the equilibrium structure, depicting the tube orientation angle φ. (b) The Binding energy of a (7,0) Bi-NT array as a function of the intertube spacing a_0. (c) Dependence of the array binding energy (ΔE) on the orientation angle φ of individual nanotubes.

S3. Other possible intertube bonding geometries

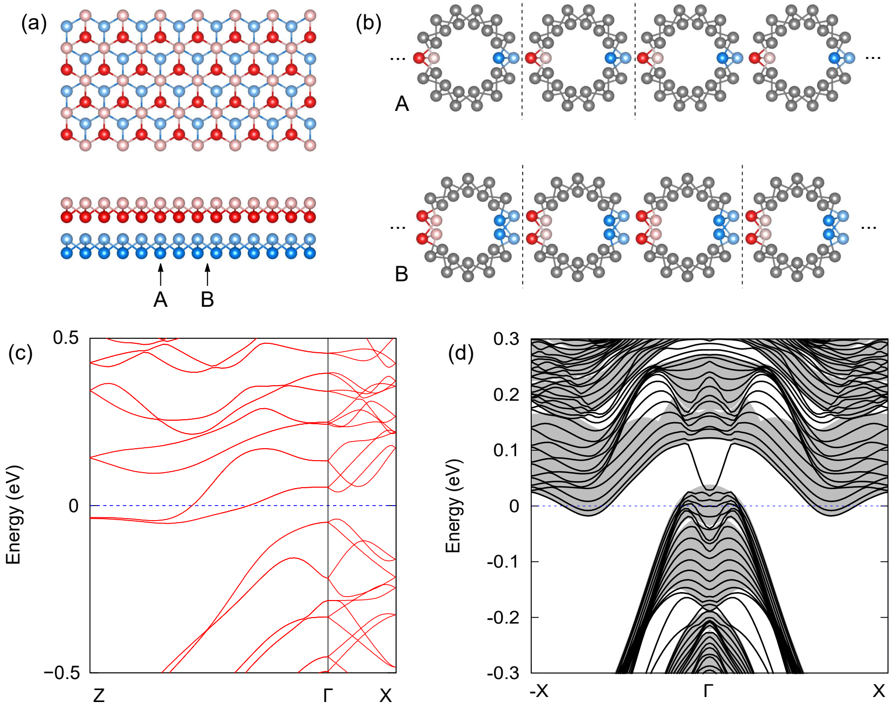

Figure S3: Bonding geometries of Bi-NT arrays. (a) Top view and side view of two Bi bilayer. (b) Different structural types of Bi-NT arrays. Using (7,0) Bi-NT, the two simple types of arrays that are typically rolled from a Bi bilayer sheet at point A or B in (a). Dashed lines represent the unit cell of Bi-NT array. Type B is only more stable by 1meV/atom. (c) Calculated band structure of type B Bi-NT array. (d) Energy dispersion of edge states for the Bi-NT array nanoribbon of type B.

S4. The robustness of QSH phse against the structural disorder

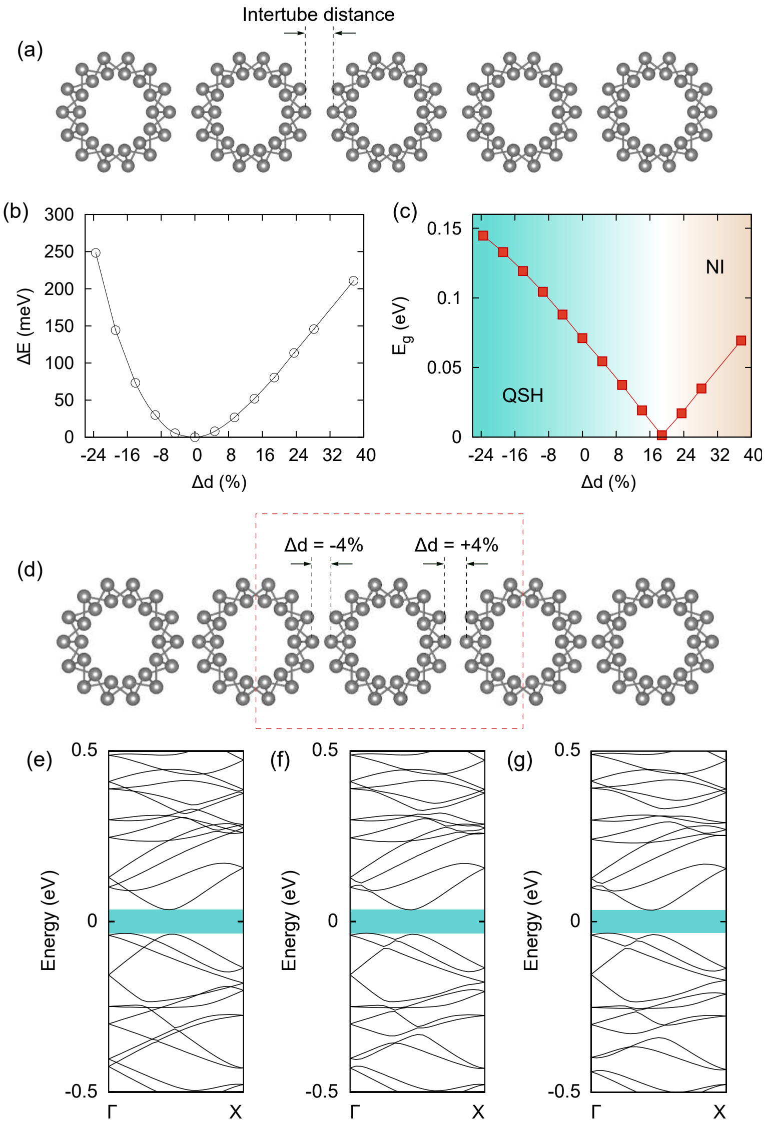

Figure S4.1: (a) The (7,0) Bi-NT array with varying intertube distance. (b) Calculated total energy difference (ΔE) and energy gap (E_g) as a function of intertube distance. There is a topological phase transition from QSH to normal insulator (NI) at +19% intertube distance. (d) Atomic structure of disordered Bi-NT array. There are two different intertube spacings in the double-sized supercell along x direction. Calculated band structure of (e) pristine and (f) ±4% and (g) ±8% disordered (7,0) Bi-NT array. The band structure near Fermi level is quite robust against the structural disorder.

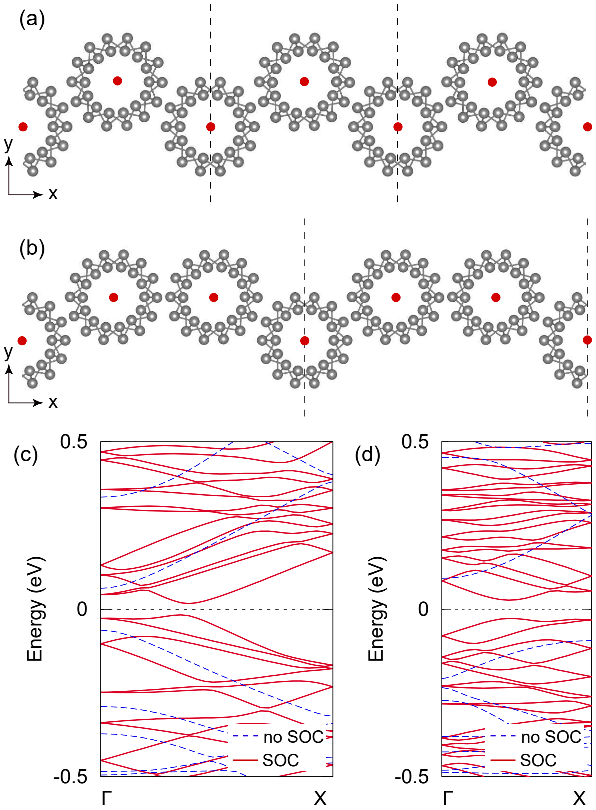

Figure S4.2: (a), (b) The side view of modeled ripple structures using (7,0) Bi-NT. The dashed line indicates unit cell along the *x* direction. The dots indicate the center of nanotubes. (c), (d) The calculated band structures for the ripple structures (a) and (b), respectively. Both structures are extreme cases that whole area is covered by the rippled structure. Even for this extreme condition, the topological phase is still preserved with a topological gap ∼34 meV and ∼54 meV for the ripple structure in (a) and (b), respectively.

S5. Strucutural stability of Bi-NT

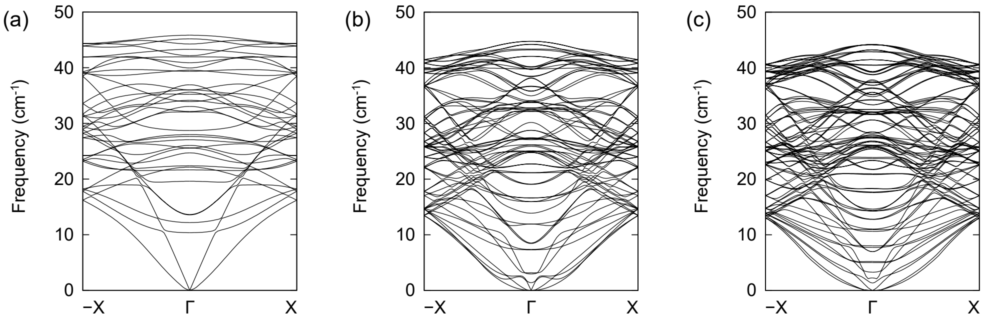

Figure S5.1: (a)-(c) Calculated phonon band dispersions for pristine (7,0), (13,0), (17,0) Bi-NT, respectively. No imaginary frequency is observed, supporting the structural stability of Bi-NTs.

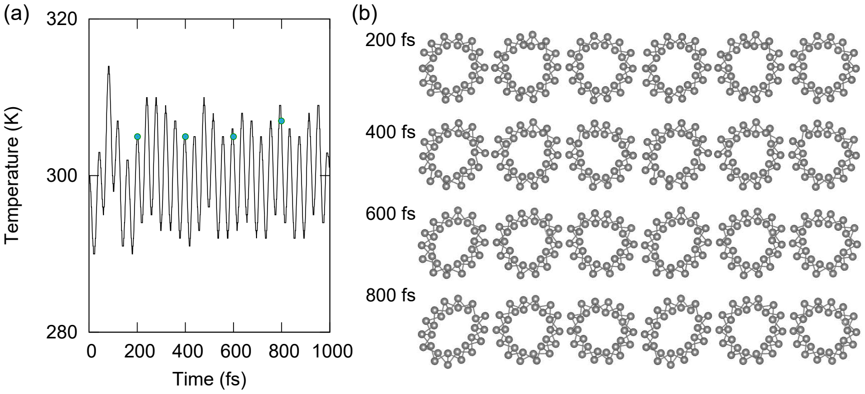

Figure S5.2: *Ab initio* molecular dynamics (MD) simulation for (7,0) Bi-NT array. (a) Temperature variation with time, and the green dots denote the times of snap shots taken in (b). We used a tripled unit cell along the x direction and the MD simulations are done using canonical ensemble at 300 K. (b) Snap shots of the structures at different times, demonstrating the stability of (7,0) Bi-NT array at room temperature.

S6. The calculated Z_2 topological invariant of Bi-NT arrays

For the numerical computation of Z_2 invariants, several approaches have been proposed. Here we follow the approach introduced by Soluyanov and Vanderbilt [1]. This method can be applied to cases without inversion symmetry. To describe Z_2 invariants, we first introduce the time-reversal polarization as [2]

$$P_\theta = P^I + P^{II}, \tag{1}$$

where $P^S = \oint_{BZ} A^S(k)\, dk$, with Berry connection $A(k) = i\sum_n \langle u_{nk}|\partial_k|u_{nk}\rangle$ and $S = I$ or II for a system whose occupied bands split into two groups (I and II) which are time-reversal partners with each other. The topological invariant can be described by an adiabatic pumping of time-reversal polarization between t=0 and T/2

$$Z_2 = P_\theta(T/2) - P_\theta(0)\text{mod}(2). \tag{2}$$

We can rewrite equation (2) in terms of the Wannier charge centers (WCCs). The charge polarization is related to the position of Wannier functions (WFs) in a subsystem, and the time-reversal polarization can be understood as the adiabatic shift of WFs. The WFs associated with the lattice vector R can be written as

$$|R, n\rangle = \frac{1}{2\pi}\int_{-\pi}^{\pi} dk e^{-ik(R-x)}\,|u_{nk}\rangle\,. \tag{3}$$

The WCC for the n-th state, $\bar{x}_n$, can be defined as the mean value of $\langle 0n|\hat{X}|0n\rangle$, where $\hat{X}$ is the position operator and $|0n\rangle$ is the state corresponding to a WF in the cell with $R = 0$. Then we obtain

$$\bar{x}_n = \frac{i}{2\pi}\int_{-\pi}^{\pi} dk\,\langle u_{nk}|\partial_k|u_{nk}\rangle\,. \tag{4}$$

Taking into account that $\sum_n \bar{x}_n^S = \frac{1}{2\pi}\oint_{BZ} A^S(k)$ with $S = I$ or II, equation (2) yields

$$Z_2 = \sum_\alpha [\bar{x}^I_\alpha(T/2) - \bar{x}^{II}_\alpha(T/2)] - \sum_\alpha [\bar{x}^I_\alpha(0) - \bar{x}^{II}_\alpha(0)]. \tag{5}$$

In this pumping process when applied to a 2D topological insulator, we can define the reciprocal space with k_1 and k_2, which play the roles of k and t, respectively. Using above formalism, we can directly look at the evolution of WCCs for effective 1D systems of pumping parameter k_2 in the subspace of occupied states. At k_2=0, the WCCs appear in degenerate pairs due to time-reversal symmetry. When k_2 moves away from the origin, the WCC pairs split and recombine at k_2=π. Therefore, the evolution of each WCC pair determines the Z_2 topological invariant of system by the number of crossings between the evolution lines and the reference line. If it is odd, then the Z_2 number is odd. In our system, we can define the WCCs in k_x, k_z reciprocal space. The corresponding results for the Bi-NT arrays are shown in Fig. S6. We choose k_z as the pumping parameter.

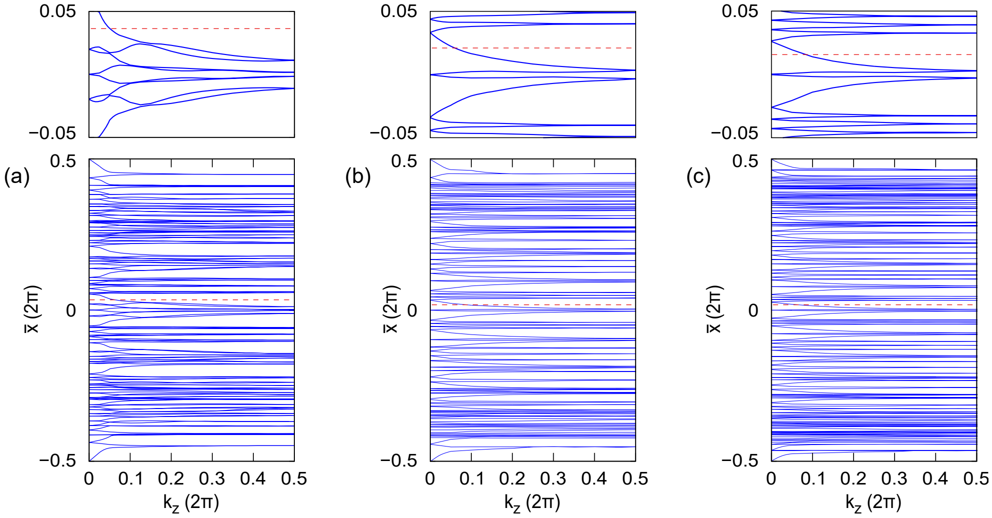

Figure S6: The Z_2 topological invariants of Bi-NT arrays. (a)-(c) Evolution of Wannier charge centers (WCCs), $\bar{x}$, as obtained for (7,0), (13,0), and (17,0) Bi-NT arrays, respectively, by varying the pumping parameter k_z. Upper panels are enlarged WCCs near $\bar{x} = 0$. The evolution curves (blue solid line) cross an arbitrary reference line (red dashed line) odd number of time. The odd number of crossings indicates that the Kramer pairs with time-reversal-invariant momenta exchange their partners during the pumping process, so that the corresponding system is a nontrivial phase.

S7. The band structure using hybrid functional HSE06

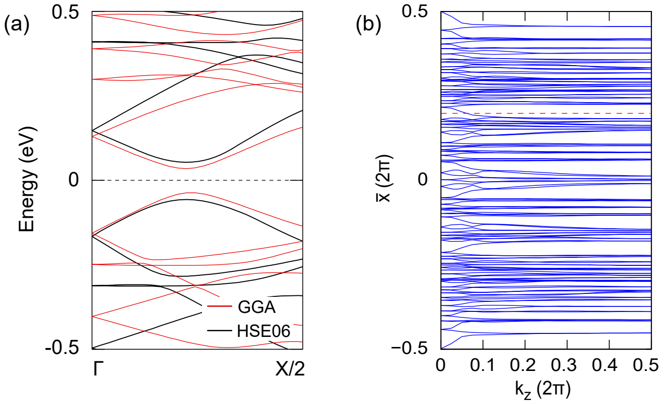

Figure S7: (a) The calculated band structure of (7,0) Bi-NT array using the GGA and HSE06 functional for comparison. The GGA band gap (70 meV) is about 30% smaller than the HSE06 band gap (104 meV). (b) Evolution of WCCs for (7,0) Bi-NT array using HSE06 functional.

S8. Effective model for Bi-NT array

The effective Hamiltonian for the Bi-NT array system can be constructed by applying a perturbative $k \cdot p$ theory to quantitatively describe the bulk states near the Γ point, albeit using molecular orbital wavefunctions instead of atomic orbital wavefunctions as done conventionally before [3]. Specifically, the states are mainly contributed by four hybridized states of Bi-NT molecular orbitals, denoted as $(|\Psi,\uparrow\rangle, |\Psi^*,\uparrow\rangle, |\Psi,\downarrow\rangle, |\Psi^*,\downarrow\rangle)$, where Ψ, Ψ^* stand for a bonding and anti-bonding molecular orbital, respectively. The Hamiltonian is written as

$$H(\vec{k}) = \epsilon_0 I_{4\times4} + \begin{bmatrix} M(\vec{k}) & Ak_x & i\alpha_R k_x & \triangle_c \\ Ak_x & -M(\vec{k}) & -\triangle_c & -i\alpha_R k_x \\ -i\alpha_R k_x & -\triangle_c & M(\vec{k}) & -Ak_x \\ \triangle_c & i\alpha_R k_x & -Ak_x & -M(\vec{k}) \end{bmatrix}, \tag{6}$$

where $\epsilon_0 = C + Dk^2$, $M(\vec{k}) = M - Bk^2$, and $k^2 = k_x^2 + k_z^2$, with $A, B, C, D, \alpha_R, \triangle_c$ and M beging the model parameters. We consider the Rashba SOC, α_R, to account for the Rashba effect along x direction and the effect of inversion symmetry through $\triangle_c$. For M/B <0, the system is in the normal phase [Fig. S8(a)]. As $\mid M \mid$ decreases, the gap decreases until it closes at M=0 as shown in Fig. S8(b). For M/B >0, the gap opens again, the bonding and anti-bonding band inversion is induced, leading to a topological phase as illustrated in Fig. S8(c).

Topological order depends on the sign of parameter M, which is related to SOC strength parameter λ_{so} in the MS. In the first-principles calculation, the SOC can be included as a perturbation in the scalar relativisitic Hamiltonian with a self-consistent treatment at each variational step. The total Hamiltonian of system is given by

$$H = H_0 + H_{SO} \tag{7}$$

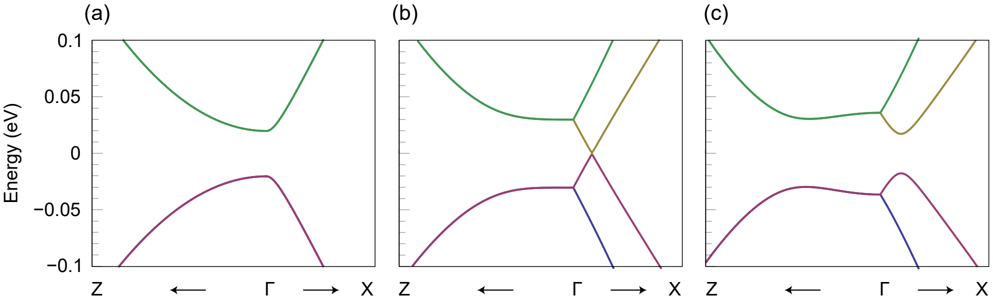

Figure S8: Energy dispersion of the effective model with parameter $A = -3.62$ eV, $B = -18$, $C = 0$ eV, $D = -0.594$ eV, (a) for normal insulating phase $\alpha_R = 0$ eV, $\triangle_c = 0$ eV and $M = 0.02$ eV; (b) for phase transition point $\alpha_R = 0.9$ eV, $\triangle_c = 0.03$ eV and $M = 0$ eV; (c) for topological insulating phase $\alpha_R = 1.2$ eV, $\triangle_c = 0.03$ eV and $M = -0.02$ eV.

where H_0 is the scalar relativistic Hamiltonian and H_{SO} is the spin-orbit Hamiltonian, which has the form

$$H_{SO} = \frac{\hbar^2}{2m^2c^2}\frac{1}{r}\frac{dV}{dr}\vec{L}\cdot\vec{\sigma} = \lambda_{so}\vec{L}\cdot\vec{\sigma}, \tag{8}$$

λ_{so} is the SOC strength. We can perform DFT calculations to artificially tune λ_{so} by changing light velocity c. With increasing λ_{so}, we can find the critical SOC at the gap closing point, which corresponds to $M = 0$ in the effective model.

S9. The molecular bonding vs. antibonding orbitals of Bi-NTs

For the distinction between atomic orbital inversion and molecular orbital inversion, we further studied the topological phase transition in single Bi bilayer (atomic band inversion) [Fig. S9(a)] vs. (13,0) Bi-NT (molecular band inversion) [Fig. S9(b)]. Fig. S9(c),(d) shows the calculated band structure and squared-wave function of the valence and conduction band at the Γ point for single Bi bilayer. The p orbitals of two bismuth atoms in a unit cell forms the bonding and antibonding state with definite parity ($\pm$). Without SOC, the valence band composed of bonding Bi $p^{+}_{x\pm iy}$ orbitals while conduction band composed of antibonding Bi p^{-}_{z}. When we further take into account the effect of SOC, these band orders are inverted [Fig. S9(d)]. For the Bi-NT, the form of cylindrical bismuth molecules, we also did same calculation using (13,0) Bi-NT [Fig. S9(e),(f)]. Without SOC, we can clearly see the bonding and antibonding molecular states from a linear combination of many Bi $p_{x,y}$ and p_z orbitals, respectively. The valence and conduction bands are no longer composed of single atomic orbital. When we considered SOC in Bi-NT, these molecular bonding and antibonding character are inverted. We can applied these molecular orbitals to Bi-NT array system and found that topological phase transition is related with molecular orbital inversion.

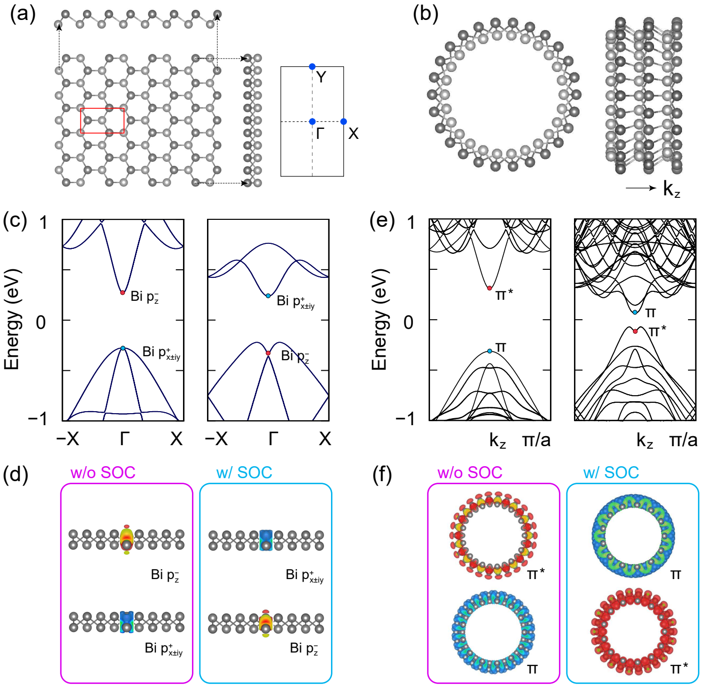

Figure S9: (a) Atomic structure of single Bi bilayer with rectangular unit cell and corresponding Brillouin zone. (b) Atomic structure of single (13,0) Bi-NT. (c) Calculated band structure of single Bi bilayer without SOC (left panel) and with SOC (right panel). (d) Squared single atomic wave-function of the conduction and valence states as indicated by dots in (c) without SOC and with SOC, respectively. (e) Calculated band structure of (13,0) Bi-NT without SOC (left panel) and with SOC (right panel). (f) Squared molecular wave-function of the conduction and valence states as indicated by dots in (e) without SOC and with SOC, respectively.

S10. The charge redistribution at the junction point

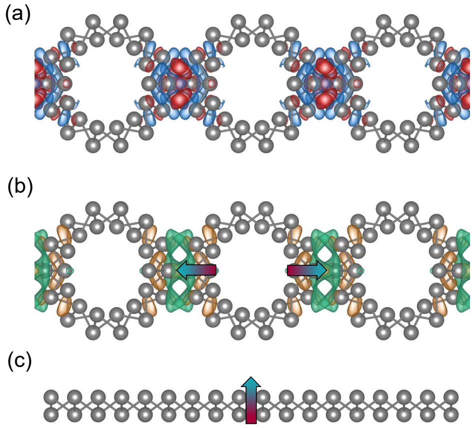

Figure S10: Charge redistribution of Bi-NT arrays. (a) Charge accumulation (red) and depletion (blue) of a (7,0) Bi-NT array. The induced charge density $\Delta\rho = \rho$ [(7,0) Bi-NT array] $-$ ρ [pristine (7,0) Bi-NT] relative to the charge densities obtained when Bi-NTs are decoupled completely. (b) The potential difference $\Delta V = V$ [(7,0) Bi-NT array] $-$ V [pristine (7,0) Bi-NT] of a (7,0) Bi-NT array. Yellow (green) surfaces correspond to a positive (negative) induced potential. Due to redistribution of charge density, an electric field (out of tube direction) is induced at the junction point. (c) Effectively the case is similar to a single Bi bilayer under electric field.

S11. The localization length of edge states

To determine the localization length of topological edge state, we use the BHZ Hamiltonian [3-4] in the low-energy regime as

$$H_{BHZ}(\vec{k}) = \begin{bmatrix} h(\vec{k}) & 0 \\ 0 & h^*(-\vec{k}) \end{bmatrix}, \tag{9}$$

$$h(\vec{k}) = \epsilon(k) I_{4\times4} + \vec{k}\cdot\vec{\sigma} \tag{10}$$

$$\epsilon(k) = C - Dk^2, \quad \vec{d}(k) = [Ak_x, Ak_y, m(k)], \tag{11}$$

$$m(k) = M - Bk^2, \quad k^2 = k_x^2 + k_y^2, \tag{12}$$

where A, B, C, D and M are material parameters. Here, $I_{2\times2}$ is a 2×2 unit matrix, $\vec{\sigma}$ is the Pauli matrix. The general solution for the edge states can be derived analytically. We deal with a system on a half plane. By putting a trial solution $\psi = e^{\lambda y}$ into the Schrödinger equation

$$H_{BHZ}(k_x, -i\partial_y)\psi = E\psi, \tag{13}$$

the secular equation is

$$\det \mid H_{BHZ}(k_x, -i\lambda) - E \mid = 0, \tag{14}$$

which gives four solutions of $\pm\lambda_1$ and $\pm\lambda_2$,

$$\lambda_{1,2} = \sqrt{k_x^2 + F \pm \sqrt{F^2 - (M^2 - E^2)/(B_+B_-)}}, \tag{15}$$

where $F = \frac{A^2 - 2(BM+DE)}{2B_+B_-}$ and $B_\pm = B \pm D$. If we apply a boundary condition as

$$\psi(y=0) = 0 \quad \text{and} \quad \psi(y\to\infty) = 0, \tag{16}$$

one can get

$$\lambda_1\lambda_2 = \frac{BM+DE}{B_+B_-} - k_x^2, \quad \lambda_1+\lambda_2 = \frac{DM+BE}{k_xB_+B_-}. \tag{17}$$

Combine (17) with (15) , one gets the dispersion of edge states

$$E = -DM/B \pm A\sqrt{B_+B_-/B^2}k_x. \tag{18}$$

The dispersion shows a massless Dirac cone with the Fermi velocity $v_F = (A/\hbar)\sqrt{B_+B_-/B^2}$. From equation (17) and (18), one can get

$$\lambda_{1,2} = \frac{M}{B} + \frac{2DG}{B}k_x - k_x^2, \quad \lambda_1+\lambda_2 = 2G, \tag{19}$$

where $G = \pm/(2\sqrt{B_+B_-})$. The properties of the solution for $\lambda_{1,2}$ determine the spatial distribution of the wavefunctions in real space. The edge states distribute mostly near the boundary ($y = 0$), with the scale of the decay length about $\lambda_{1,2}^{-1}$ for real $\lambda_{1,2}$, mainly determined by the larger one of the $\lambda_{1,2}^{-1}$ [4]. If we choose $\lambda_1 > \lambda_2$, λ_2^{-1} gives the physical localization length l. For example, λ_2=0, the localization length is infinite and the edge states extend to the whole bulk area. From equation (19), this appears when $k_x = k_x^{\pm} = DG/B \pm \sqrt{(DG/B)^2 + M/B}$. We note that the states at $k_x = k_x^{\pm}$ are located at the band edge of the projection of the bulk band and, at these points, the edge dispersion is tangential to the bulk band projection. We can rewrite $\lambda_1\lambda_2 = -(k_x - k_x^+)(k_x - k_x^-)$. Then, $\lambda_2 (= l^{-1})$ is expressed as

$$l^{-1} = G - \sqrt{G^2 + (k_x - k_x^+)(k_x - k_x^-)}. \tag{20}$$

Fig. S11(a) shows the behavior of l^{-1}. At the points where edge state merging with bulk band, $P_\pm(k_x = k_x^{\pm})$, l goes to infinite. l has the minimum value at $k_x = (k_x^+ + k_x^-)/2$, with l_{min}=$1/[G - \sqrt{G^2 - (k_x^+ - k_x^-)^2/4}]$. When $G = (k_x^+ - k_x^-)/2$, l_{min}=$2/(k_x^+ - k_x^-)$. Therefore, l^{-1} is approximately given by the k-space distance between the two points P_+ and P_-.

In the Bi-NT arrays, the localization length of the edge states can be calculated using

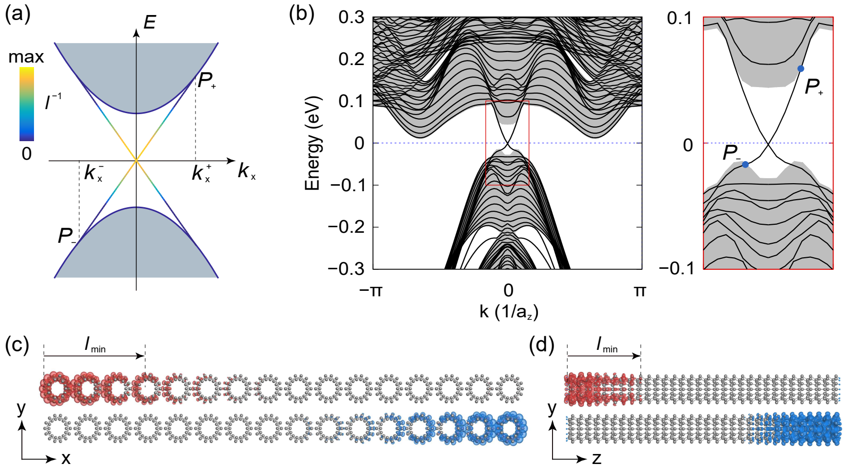

Figure S11: (a) Localization length l for the effective model with energy dispersion. Shaded regions denote the energy spectrum of bulk. The color indicates the inverse of l at each k point. (b) Energy dispersion of edge states for the structure of nanoribbons made of a finite number of 16 Bi-NTs of infinite length for the side-termination. Left panel is the enlargement of the bands near the point where the points representing the edge states merged into bulk state. (c),(d) The charge distribution of edge states at the Dirac point for side- and end-termination, respectively. The calculated minimum localization length ($l_{min}\sim$4.36 nm for side-termination and $l_{min}\sim$3.68 nm for end-termination) is indicated by arrows from boundary Bi-NT.

these two points $P_\pm$ [Fig. S11(b)]. From the band structure, we can get $k_x^+= 0.28$ nm^{-1} and $k_x^-= -0.18$ nm^{-1}. The calculated l_{min} for edge states of side-termination Bi-NT array is ∼4.36 nm. Comparing charge distribution of edge state, this minimum localization length corresponds to a distribution of edge state across ∼ 4 nanotubes [Fig. S11(c)]. For the end-termination, we can get $k_x^+= 0.61$ nm^{-1}, $k_x^-= -0.48$ nm^{-1} and $l_{min}\sim$3.68 nm [Fig. S11(d)]. Moreover, the localization length determines the minimal width of the system required for electrical contacts of transport measurement.

S12. The QSH phase of various Bi-NT arrays

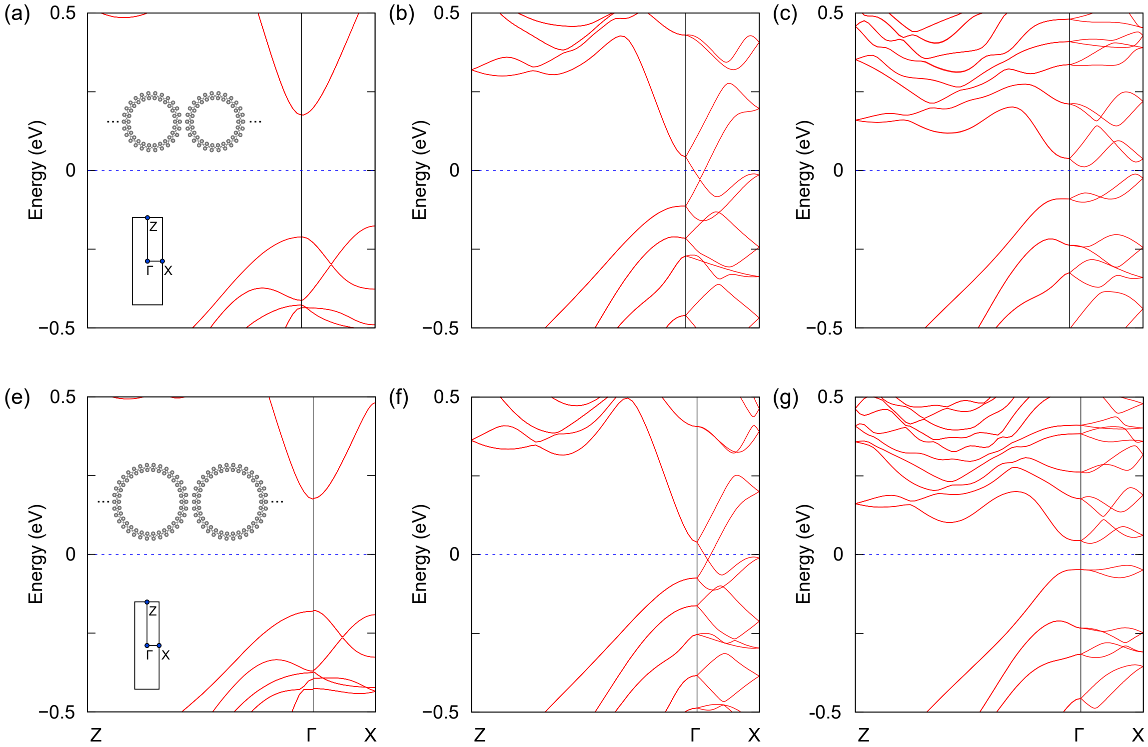

Figure S12: The QSH phase of various Bi-NT arrays. (a)-(c) Band structure as the SOC strength is changed from 0 to 0.7, and to 1 of the true value in (13,0) Bi-NT array. (e)-(g) Band structure as the SOC strength is changed from 0 to 0.63, and to 1 of the true value in (17,0) Bi-NT array.

S13. The calculated band structure of Bi-NT arrays on the BN sheet.

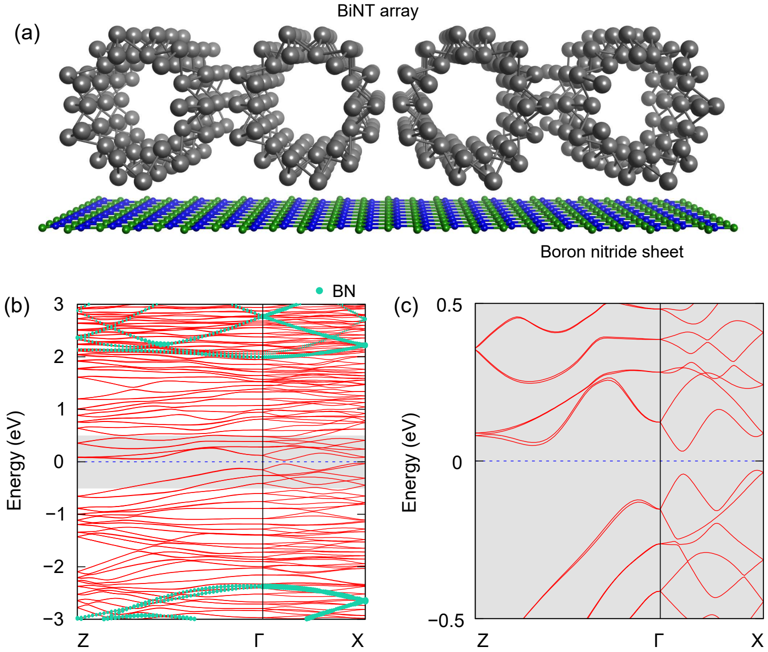

Figure S13: Topological robustness of Bi-NT arrays on insulating boron nitride (BN) substrate (sheet). (a) Schematic structure of (7,0) Bi-NT array on the BN substrate. (b) Calculated band structure of (7,0) Bi-NT on the BN sheet. Shaded region in (b) is enlarged in (c). Non-trivial character of (7,0) Bi-NT array is still preserved on the BN substrate.

S14. The non-trivial edge state of curved Bi-NT array

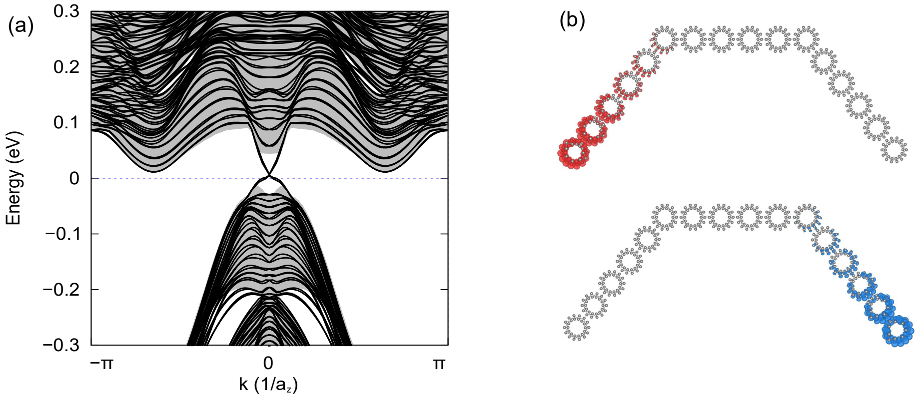

Figure S14: The robustness of topological edge state of curved Bi-NT array. (a) The topological edge state for the (7,0) Bi-NT nano-array structure for curved geometry shown in (b). (b) The real space charge distribution of topological edge states at the Dirac point are shown with an isosurface of 2×10^{-4} e/Å^3.

References

(1) A. A. Soluyanov, and D. Vanderbilt, Phys. Rev. B **83**, 235401 (2011).

(2) L. Fu, and C. L. Kane, Phys. Rev. B **74**, 195312 (2006).

(3) B. A. Bernevig, T. L. Hughes, and S. C. Zhang, Science **314**, 1757 (2006).

(4) B. Zhou, H.-Z. Lu, R.-L. Chu, S.-Q. Shen, and Q. Niu, Phys. Rev. Lett. **101**, 246807 (2008).